metals

MDPI

Article

High Strain Rate Behavior of Ultrafine Grained AA2519 Processed via Multi Axial Cryogenic Forging

Amin Azimi [1,*], Gbadebo Moses Owolabi [1], Hamid Fallahdoost [2], Nikhil Kumar [1] and Grant Warner [1]

[1] Department of Mechanical Engineering, Howard University, Washington, DC 20059, USA; gbadebo.owolabi@howard.edu (G.M.O.); nikhil.kumar@howard.edu (N.K.); g_warner@howard.edu (G.W.)
[2] Department of Mechanical Engineering & Materials Science and Engineering Program, Binghamton University (SUNY), Binghamton, NY 13902, USA; Hfallah1@binghamton.edu
* Correspondence: amin.azimi@bison.howard.edu or aminazimi.kntu@gmail.com; Tel.: +1-202-806-6594

Received: 27 December 2018; Accepted: 19 January 2019; Published: 23 January 2019



Abstract: The present work deals with studies on the dynamic behavior of ultrafine grained AA2519 alloy synthesized via cryogenic forging (CF) and room temperature forging (RTF) techniques. A split-Hopkinson pressure bar was used to perform high strain rate tests on the processed samples and the microstructures of the samples were characterized before and after impact tests. Electron backscatter diffraction (EBSD) maps demonstrated a significant grain size refinement from ~740 nm to ~250 nm as a result of cryogenic plastic deformation showing higher dislocation densities and stored strains in the CF sample when compared to the RTF sample. This microstructure modification caused the increase of dynamic flow stress in this alloy. In addition, the aluminum matrix of the CF alloy is more densely populated with fragmented particles than the RTF alloy due to the heavier plastic deformation applied to the cryogenically forged alloy. The results obtained from the stress–strain curve for the RTF sample showed intense thermomechanical instabilities in the RTF sample which led to a severe thermal softening and the subsequent sharp drop in the flow stress. However, no significant decrease was observed in the stress–strain curve of the CF alloys with ultrafine grains which means that thermal softening would probably not be the most effective failure mechanism. Furthermore, higher level of sensitivity of CF alloys to strain rates was observed which is ascribed to transition of rate-controlling plastic deformation mechanisms. In the post-mortem microstructure investigation, deformed and transformed adiabatic shear bands (ASBs) were identified on the RTF alloy when the strain rate is over 4000 s^{-1} at which it had experienced a significant thermal softening. On the other hand, circular path and aligned split arcs are the various shapes of the deformed ASB seen at no earlier than 4500 s^{-1} in the CF alloys. This is associated with the crack failure caused by grain boundary sliding.

Keywords: ultrafine grained AA2519; cryogenic forging; high strain rates; adiabatic shear bands; split-hopkinson pressure bar

1. Introduction

Strain-hardenable aluminum alloys such as AA2519 have progressively been considered as one of the prime engineering materials for aircraft and automotive structural components due to their unique mechanical properties such as high strength-to-weight ratio, excellent ductility, good machinability, and high corrosion resistance [1,2]. With regard to reducing fuel consumption, an ever-growing demand for high specific strength materials in the aircraft and the automotive components has led researchers to investigate potential techniques to enhance the strength of the aluminum alloys [3,4]. To this end, the superior mechanical properties of nanostructured (NS) and

ultrafine grained (UFG) aluminum alloys have motivated a worldwide interest toward developing grain refinement methods [2,5,6]. Severe plastic deformation (SPD) techniques are believed to be promising top-down approaches in attaining extremely refined grain size aluminum alloys with homogenized equiaxed microstructure [7]. During SPD process, a high level of plastic strains is applied without a significant dimension variation which makes it feasible to govern the microstructure and the mechanical characteristics of the aluminum alloys. Integration of high hydrostatic pressure and large shear strains provides the required conditions to create high densities of crystal lattice defects such as dislocations leading to a significant refinement of the grains [8,9]. The commonly employed SPD techniques are high pressure torsion (HPT) [10], equal channel angular pressing (ECAP) [11], accumulative roll bonding (ARB) [12] and multi axial forging (MAF) [13]. Among SPD methods, MAF is a least-cost deformation technique in which the material undergoes frequent forging processes in three orthogonal directions such that the original geometry of the material remains unchanged with minimum distortion even after multiple cycles [14]. Homogeneous microstructure and improved mechanical properties were observed as a result of MAF [15]. However, due to recrystallization and dynamic recovery of grains during the plastic deformation, SPD at room temperature cannot be very effective to develop UFG materials [16]. Thus, dynamic recovery which is associated with high/medium stacking fault energy metals and alloys limits the generation of dislocation boundaries and hinders grain refinements [15]. The reports of previous research studies showed that SPD at cryogenic temperature has a substantial effect in refining the microstructure [17]. At the liquid nitrogen temperature, dynamic recovery is suppressed which leads to accumulate high density of dislocations and the formation of ultrafine grains [14]. Accordingly, cryogenic SPD requires less amount of plastic deformation energy for generating UFG structure in comparison with the SPD processes at room temperature [18]. There are some studies regarding microstructures and mechanical properties of aluminum alloys processed by MAF at cryogenic temperature [14,17,18]. Singh et al. [18] studied the simultaneous improvement of strength and ductility as well as the corrosion resistance of ultrafine grained AA2024 processed by multiaxial cryoforging and cryorolling followed by aging. They observed that MAF at cryogenic temperature showed a greater yield strength when compared to that obtained in the cryorolled samples. Shih et al. [19] reported a significant increase in the tensile strength of the cryogenically forged AA6066 when compared with the T6 treated samples.

The growing number of applications of aluminum alloys in both aerospace and automotive sectors in which their structural components are subjected to impact loadings such as crash, explosion, and high-speed collision highlights the importance of understanding the mechanical responses of the materials under impact loading conditions [20–22]. Unlike the quasi-static deformation process, impact and dynamic loads often involve high strain rates, large strains, and rapid changes in temperature due to severe thermoplastic heating and adiabatic deformation conditions. The deformation and failure of metallic alloys under quasi-static loading are normally by slip and twinning while failure at high strain rate is initiated by intense localization of shear strain [23–25]. As observed in previous studies, aluminum alloys indicated heterogeneous deformation leading to the formation of adiabatic shear bands (ASBs) under dynamic compressive stress [26,27]. ASBs could be defined in areas of intense shear strain localization resulted from thermo-mechanical instabilities induced by localized adiabatic heating during impact load [24,28]. The observed ASBs in aluminum alloys are commonly categorized into deformed bands including elongated grains and transformed bands formed by equiaxed ultrafine grains depending on the severity of loading [26]. Olasumboye et al. [29] have recently investigated the dynamic response and microstructure evolution of AA2219-T4 and AA2219-T6 aluminum alloys. They characterized the plastic deformation of the T4 and the T6 tempered alloys by intense shear localization at 3500 s^{-1} strain rate leading to fracture. To the best of the authors' knowledge, no literature is currently available on the formation and dynamic behavior of ultrafine grained AA2519 processed by MAF. Therefore, this research focuses on the high strain rate dynamic mechanical response of ultrafine grained AA2519 prepared by MAF at room as well as cryogenic temperatures. In addition, the microstructures of the room temperature forged (RTF) and the cryoforged (CF) AA2519 as well

as the deformed samples after the high strain rate compression tests have been investigated in order to analyze the failure mechanisms such as shear bands and cracks. These experimental data include important information on the dynamic yield and flow stresses, the strain rate sensitivity (SRS) and microstructural evolution of the alloys which can be applied in the formulation and validation of robust constitutive models for simulating the material's response at high strain rates.

2. Materials and Methods

2.1. Materials

The detailed chemical composition of the AA2519 aluminum alloy investigated in this research is summarized in Table 1. The specimens were initially homogenized at a temperature of 500 °C for 10 h in a controlled atmosphere of argon, and then quenched in water at room temperature. Samples with dimensions 33 × 31 × 28 mm^3 were cut from the prepared samples and subsequently processed through MAF.

Table 1. Chemical composition of the AA2519 aluminum alloy.

Elements	Cu	Fe	Mg	Mn	Si	Ti	V	Zn	Zr	Al
wt %	5.3–6.4	0.3	0.05–0.4	0.1–0.5	0.25	0.02–0.1	0.05–0.15	0.1	0.1–0.25	Balance

2.2. Materials Processing

The MAF process was conducted at a cryogenic temperature (i.e., liquid nitrogen temperature of −196 °C) as well as room temperature using a friction screw forging machine at a strain rate of 10 s^{-1}. The setup for cryogenic MAF consists of a Cryo-can for procuring and storing the liquid nitrogen, a sample container to hold the sample in the liquid nitrogen, and a friction screw forging machine for MAF process. To carry out MAF at cryogenic temperature, the samples were initially dipped under liquid nitrogen for 15 min. The extrusion direction of the starting samples was preferred as the first forging axis. An axial compression at an equivalent true strain of $(\Delta\varepsilon) = \ln(1/1.18) = -0.165$ was applied for one forging pass. Furthermore, quenching in liquid nitrogen for 5–10 min was performed after each pass to keep the samples in a thermal equilibrium with the liquid nitrogen. After this quenching, the samples were taken out from the containers and then immediately forged. The cumulative strain after one cycle (consisting of 3 forging passes) was obtained as $(\sum\Delta\varepsilon_{n=1}) = |\Delta\varepsilon_1 + \Delta\varepsilon_2 + \Delta\varepsilon_3| = -0.495$. The samples were rotated 90° after every pass along the axes of the applied strain in three orthogonal directions to maintain a constant dimensional ratio of 1.18: 1.11: 1.0 throughout the process. Eventually, The AA2519 samples were subjected to a cumulative strain of −2.97 under 6 cycles (18 passes). The samples were successfully forged up to 6 cycles without any cracking. Room temperature MAF processed samples were also produced and used as a reference material for this study.

2.3. High Strain Rate Tests

The processed AA2519 samples were machined to cylindrical test specimens with 3 mm diameter and 3 mm long (aspect ratio, L/D = 1). A split-Hopkinson pressure bar (SHPB) [30], also called a Kolsky bar, is used for the characterization of the dynamic response of the materials at high strain rates which fall within between 10^1 to 10^4 s^{-1} range. A schematics of the SHPB employed in performing the high strain rate tests is illustrated in Figure 1. This impact machine possesses an incident bar, a transmitter bar, a striker bar, a light gun, and data acquisition system (strain conditioners/amplifiers and a digital oscilloscope). The incident and transmitter bars are made of Ti-6Al-4V alloy and have dimensions of 13 mm in diameter and 1900 mm long. The specimens were sandwiched between the incident and transmitter bars. Strain gages of 1000 Ω resistance are mounted on the incident and transmitter bars at a distance of 940 mm away from the respective bar-specimen interfaces in order to prevent wave interference. The striker bar is fired from a pressurized gas chamber that is charged by a

regulated compressed nitrogen gas cylinder. The impact force generates elastic waves which travel through the bars and sample. The elastic wave data captured by the strain gages are processed by strain conditioners/amplifiers connected to the strain gages, and are stored by the connected mixed signal digital oscilloscope. Using these signals, the data are converted to true stress, true strain and strain rate data using a MATLAB code that was written based following equation on one dimensional wave theory [30,31]:

$$\sigma = (\frac{A_B}{A_S})E_B\varepsilon_T \quad (1)$$

$$\varepsilon = -2(\frac{C_B}{L_S})\int_0^t \varepsilon_R dt \quad (2)$$

$$\dot{\varepsilon} = -2(\frac{C_B}{L_S})\varepsilon_R \quad (3)$$

where ε_T and ε_R are transmitted and reflected strain pulses, A_B, C_B, and E_B represent cross-sectional area of the bars, wave propagation speed in the bars and elastic modulus of the bar material, respectively and A_s is the cross-sectional area of the specimens.

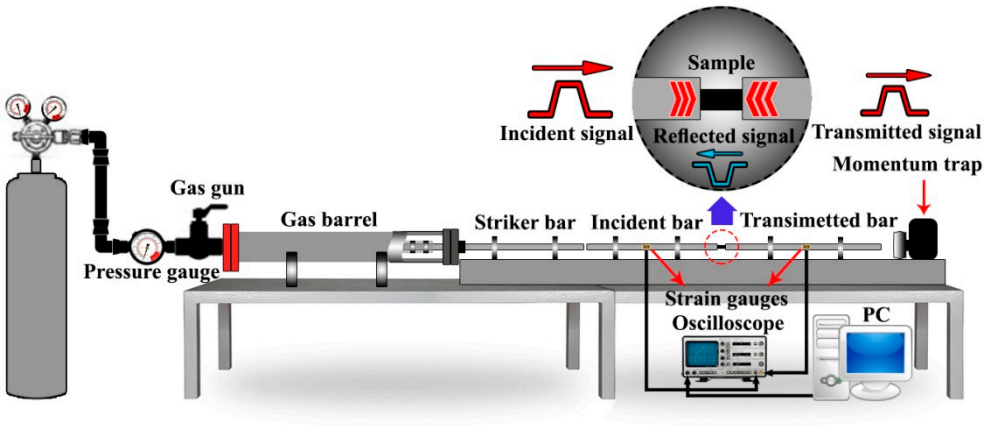


Figure 1. Schematics of the split-Hopkinson pressure bar (SHPB) employed in performing the high strain rate tests.

2.4. Microstructural Characterization

The microstructural specimens were prepared by standard metallographic grinding and mechanical polishing techniques and were etched using a solution consisting of 25 mL methanol, 25 mL HCl, 5 mL HNO_3, and a drop of HF as reagent for AA2519. Optical microscopic studies were performed by Zeiss Optical Microscope (Jena, Germany) on the prepared samples after processing and after mechanical tests. The microstructures of these samples were also characterized using scanning electron microscopy (SEM) accompanied with energy dispersion spectroscopy (EDS). Electron backscattered diffraction (EBSD) was also used to estimate the grain size of the samples after MAF processing. Zeiss SUPRA™ 40VP Field Emission SEM (Jena, Germany) with TSL-OIM EBSD Data collection was employed for the EBSD analysis. The EBSD was operated at an accelerating voltage of 20 kV, and imaging was carried out at a step size of 0.05 µm with a 15 × 15 μm^2 map size. The grain size was determined by line intercept method. EBSD samples were prepared by mechanical and cloth polishing followed by electro-polishing at −30 °C at a potential of 11 V for 90−120 s. The electro-polishing was done using solution containing 20% perchloric acid and 80% methanol, direct current (DC) power supply and reference electrode (stainless steel). Furthermore, fine cloth polishing with colloidal silica was performed to relieve the remaining stresses from the surface.

3. Results and Discussion

3.1. Initial Microstructure Characterization

The results of the microstructural characterization of the two RTF and CF of AA2519 via optical microscope (OM), SEM, and EBSD prior to dynamic mechanical loading are highlighted in Figures 2–4, respectively. The optical micrographs (Figure 2a–d) illustrate unetched and etched morphology structures of the two processed alloys which show some similarities. For instance, irregular coarse and fine second phase particles are dispersed in a continuous matrix of α-aluminum phase. However, the dimensions and the distributions of the second phase particles are different in each alloy. As can be seen in Figure 2a, the particles are irregularly distributed in the RTF aluminum matrix, whereas the second phase particles are piled together in same routes along with shear bands in CF samples (Figure 2b). This trend can be also observed in the etched microstructures (Figure 2c,d). In addition, the aluminum matrix of the CF alloy is more densely populated with fine particles when compared to the RTF alloy (Figure 2e,f). Forging at cryogenic temperatures could cause heavier plastic deformation to act on the samples' matrix. Thus, more shear stress has been generated during the cryogenic forging which leads to the breaking down of the second phase particles. The broken particles is clearly identified in the CF etched sample (Figure 2f) located inside of a shear band. The same result was reported for cryogenic forged AA6066–T6 aluminum alloys [19]. The finer secondary particles in the CF sample presumably present stronger mechanical strength due to good obstructing and retarding dislocation movement.

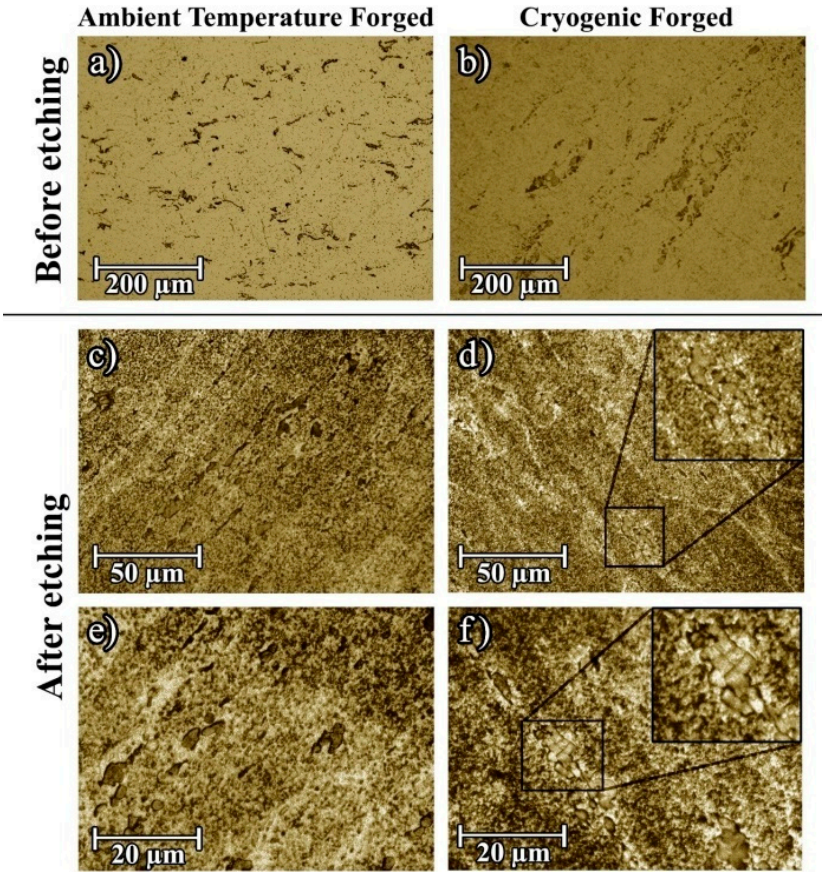


Figure 2. Optical micrographs of morphology structures in (**a**) unetched room temperature forging (RTF); (**b**) unetched cryogenic forging (CF); (**c**) etched RTF; (**d**) etched CF; (**e**) magnified etched RTF; and (**f**) magnified etched CF processed alloys.

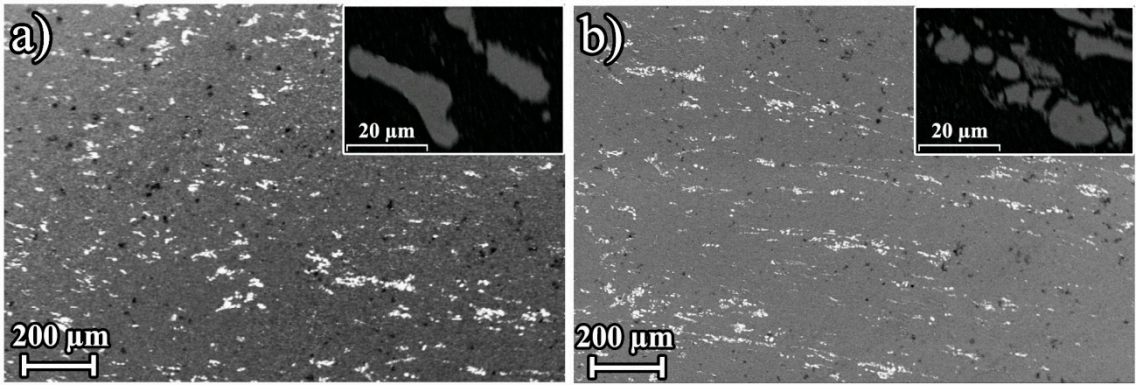


Figure 3. Backscattered SEM images of Al matrix in the (**a**) RTF and (**b**) CF samples with second phase configuration at higher magnifications.

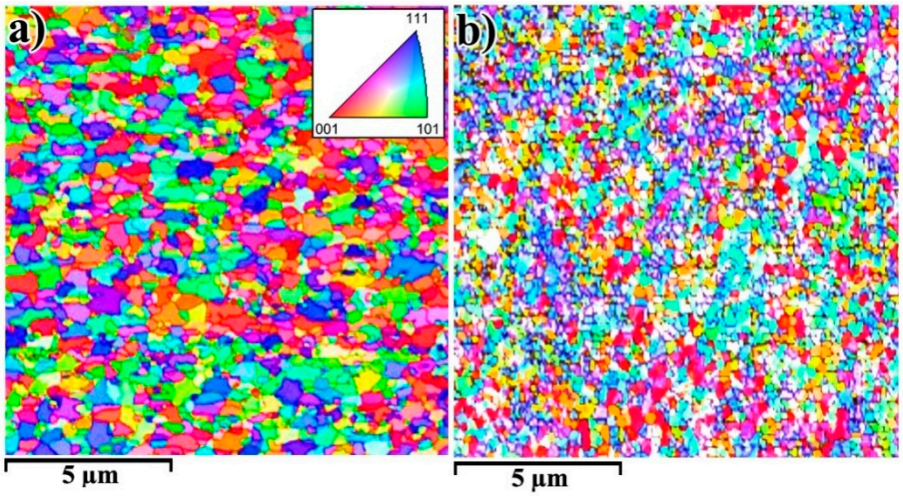


Figure 4. Electron backscatter diffraction (EBSD) maps of the (**a**) RTF and (**b**) CF deformed specimens.

Figure 3 is illustrates the backscattered SEM images of the Al matrix in the RTF and the CF samples with second phases at higher magnification. As discussed in aforementioned optical micrographs (Figure 2), the second phase particles are drawn in the specific direction of shear band propagation on the CF sample, while they are dispersed irregularly on the RTF microstructure. Furthermore, the magnified SEM images represent the fragmented second phase in the CF specimen due to the higher shear stress formed during the forging process. According to the measurement of EDS attached to the SEM, the phase is rich in Al and Cu which is primarily metastable AlCu(θ′, θ″) and stable Al_2Cu(θ) particles appearing as coherent and semi-coherent phases, respectively [32]. Dislocations are pinned by the dispersion of the secondary phase bringing an improving effect on the mechanical properties, especially at high temperature, for its thermal stability, nevertheless the second phase particles are widely believed to have adverse effects on the mechanical properties, due to their contribution to crack initiation, crack growth, and corrosion [33].

The EBSD maps of the deformed samples are shown in Figure 4; with Figure 4a associated with the RTF domain surface and Figure 4b is attributed to the CF alloy. Severe deformation imposed by forging can be visualized as observed in this figure. The maps are presented such that the vertical axis is parallel to the radial direction of the sample, whereas the horizontal axis is parallel to the tangential direction, i.e., the direction of forging. The microstructure of the RTF specimen confirms an average grain size of ~740 nm as observed in Figure 4a. However, this value is of course smaller than the grain size of the solution treated sample (i.e. 50–100 µm) due to the applied large plastic strain during the six cycles forging. As a result of forging at cryogenic temperature (Figure 4b), the grain size is significantly reduced to ~250 nm (in ultrafine grain size range). From this figure, it can be

observed that the microstructure of the CF samples mostly consists of much more deformed grains than that of the RTF processed samples. This indicates a much larger strain energy stored in the samples deformed at cryogenic temperature than those of the RTF samples. The heat generated by severe plastic deformation coarsened the grains. The grain coarsening has considerably been hindered as result of imposing extremely low temperature during the forging process especially in alloys with second phase. Consequently, the grain refined structure was developed by performing multiple forging at cryogenic temperature up to nano-scale grains [15]. Dynamic recovery is suppressed during the forging process at the liquid nitrogen temperature which preserves a high density of dislocations generated and piled up by deformation, which can act as the potential recrystallization sites. Similar observations were made by Ref. [18] in which the cryogenic deforming of aluminum alloys resulted in a grain refinement of microstructure by partial dynamic recrystallization in the alloy. In addition, The EBSD images demonstrated a homogenized equiaxed grains structure without any specific direction. This is why the cryogenic multiaxial forging usually shows a larger improvement in the mechanical properties compared to that of the cryorolled Al alloys with high aspect ratio grains.

3.2. Dynamic Mechanical Behavior

In this section, the dynamic mechanical responses of the RTF and the CF samples were discussed and compared. Figure 5 is the result of the RTF-AA2519 aluminum alloy impact test. The true stress–true strain curves for the alloy at five different strain rates are indicated in Figure 5a. The stress–strain curves show an initial elastic deformation that is quickly overshadowed by a plastic deformation. Beyond the yield point, there is a stress increment with a declined rate in the plastic part which is differentiated by strain hardening to the maximum true strains of 0.09, 0.13, 0.15, 0.17, and 0.22 at 500, 1500, 2500, 3500, and 4000 s^{-1}, respectively. As observed, the strain hardening continued to the longer strain at higher strain rates. The strain hardening is a consequence of dislocation pile-ups while the materials deformed plastically. This strengthening mechanism in metallic alloys caused by accumulated dislocation density has been extensively investigated [23,34,35].

At a strain rate of the 500 s^{-1}, the sample reached the failure point immediately after the strain hardening step. However, the flow stress over the strain rate range of 1500 s^{-1} was sharply dropped depending on the strain rate, due to thermomechanical instabilities resulting from the intense adiabatic heating in some narrow local regions of the specimens at high strain rates. The conversion of the deformation energy to thermal energy has been expressed as the main reason for the heat generation which led to thermal softening [35]. Therefore, strain hardening and thermal softening phenomena and their individual force fighting for dominance during the impact deformation prescribes the maximum peak flow stress as well as the overall deformation profile [26]. Subsequently, an obvious mechanism changes from strain rate of 2500 s^{-1} was experienced. After 2500 s^{-1}, the RTF-AA2519 alloy exhibited a two-stage strain-hardening as well as flow softening before the eventual sharp drop in stress leading to failure. The multiple peaks in the stress–strain curves can be attributed to the integrated effects of dislocation accumulation and annihilation due to dynamic recovery or dynamic recrystallization [36]. After the initial softening stage, dislocation climb and cross-slip resulted in increasing dislocation dynamics and pile-ups at obstacles such as grain boundaries, Cottrell–Lomer locks and precipitates [37]. Dislocations pile-ups impose back stress which resists the movement of on-coming dislocations. Eventually, strain hardening mechanism begins to dominate again leading to an enhancement in the stress up to the second flow stress peak. Then, the stress–strain curve reached its second peak as long as the domineering effect of thermal softening up to the failure point. This trend was identified for strain rate of 4000 s^{-1}, even though there is a longer softening step causing the intense drop in stress flow without any secondary strain hardening. The large amount of generated heat and subsequent high adiabatic shear localization during the high speed plastic deformation is responsible for this substantial softening phenomenon.

Figure 5b data were extracted from the flow stress graph of the RTF prepared samples showing a notable strain rate dependency of the maximum value of flow stress as a function of strain rate.

This curve indicates a non-linear enhancement of the maximum flow stress with increase in the strain rate up to 3500 s^{-1}. This can be linked to an increase of the strain hardening at higher dynamic strain rates in comparison with quasi-static compression. From 500 s^{-1} to 3500 s^{-1}, the increase in dislocation density, distinctive dislocation loops, and sub-structures resulted in the enhancing strain hardening and flow stress peak. A decrease in the stress–strain response occurred in further strain rate. At 4000 s^{-1}, a drop in peak flow stress was experienced which is attributed to the intense of thermal softening at high impact momentums. As Figure 5c shows, the percent elongation was also increased in higher strain rate and this trend was more significant after 3500 s^{-1} which depends on the involved microstructural processes.

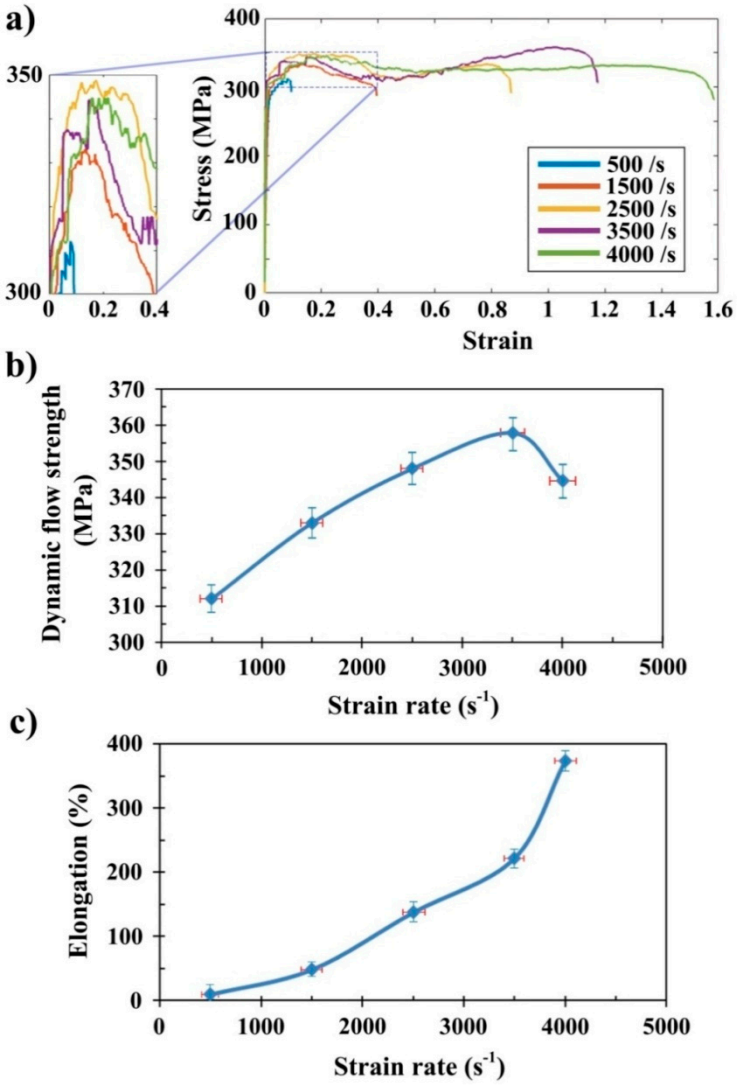


Figure 5. (**a**) Dynamic true stress–true strain curves; (**b**) dynamic flow strength variation; and (**c**) elongation percent of RTF-AA2519 with strain rate.

Similarly, Figure 6 indicates the dynamic mechanical response of the CF samples inferred from stress–strain curves and their extracted information. However, it seems that they have only one flow stress peak consisting of an initial strain hardening. Since the UFG materials are already severely deformed, they could not experience a high level of strain hardening. Furthermore, above 3500 s^{-1}, the two competitors' plasticity mechanisms (strain hardening and thermal softening) are going almost equally from yielding point up to the failure. It can be concluded that the thermal softening and shear strain localization cannot significantly affect the flow stress more than the strain hardening

in the ultrafine grained alloys. In addition, there is no considerable increase of the maximum flow stress observed above 3500 s^{-1} strain rate (Figure 6b) due to lack of significant strain hardening effect. Similar to the RTF samples, the elongation in CF alloys is completely dependent on the strain rate and it increased at higher impact momentums such that the ascending trend is going to higher rate after 3500 s^{-1} as depicted in Figure 6c.

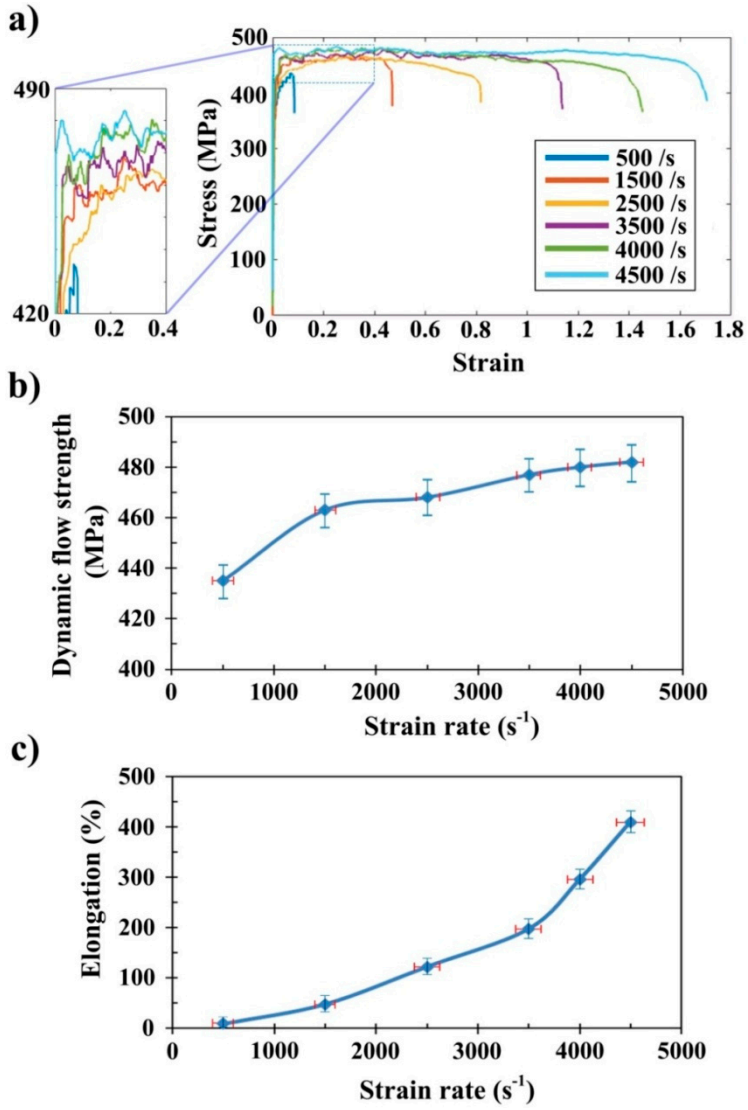


Figure 6. (**a**) Dynamic true stress-true strain curves; (**b**) dynamic flow strength variation; and (**c**) elongation percent of CF-AA2519 with strain rate.

The dynamic behavior of the RTF-AA2519 and CF-AA2519 were exhibited in comparing format in Figure 7 at 2500, 3500, and 4000 s^{-1} to realize the influence of the grain refinement to ultrafine ranges on their dynamic behavior. As seen in Figure 7, CF alloys show a higher flow stress in all three strain rate when compared to that of the RTF samples associated with a slight loss of their ultimate strain which is probably retrievable by post heat treatment. At 2500, 3500, and 4000 s^{-1} strain rates, the peak flow stresses are 348, 358, and 344 MPa for RTF and 468, 477, and 480 MPa for CF samples respectively. These data demonstrated 34, 33, and 40 percent increment in the maximum flow stress of the CF sample compared to the RTF counterpart at 2500, 3500, and 4000 s^{-1} strain rates. This dynamic strength increment can be due to the reduction in the crystallite size during the MAF process. As discussed in the microstructure analysis, the grain size decreases from 50–100 μm in solution treated samples to ~740 nm in the RTF samples and significant further reduction to ~250 nm

in the CF samples. A large amount of grain boundaries developed inside the ultrafine grains act as a barrier for motion of dislocations and facilitate their accumulation in grains resulting in an increase of their strength which is very well described with the Hall–Petch strengthening mechanism [38]. In addition, the grain refinement to ultrafine ranges indicates little destructive effect on the elongation of the AA2519 alloys under the impact loads.

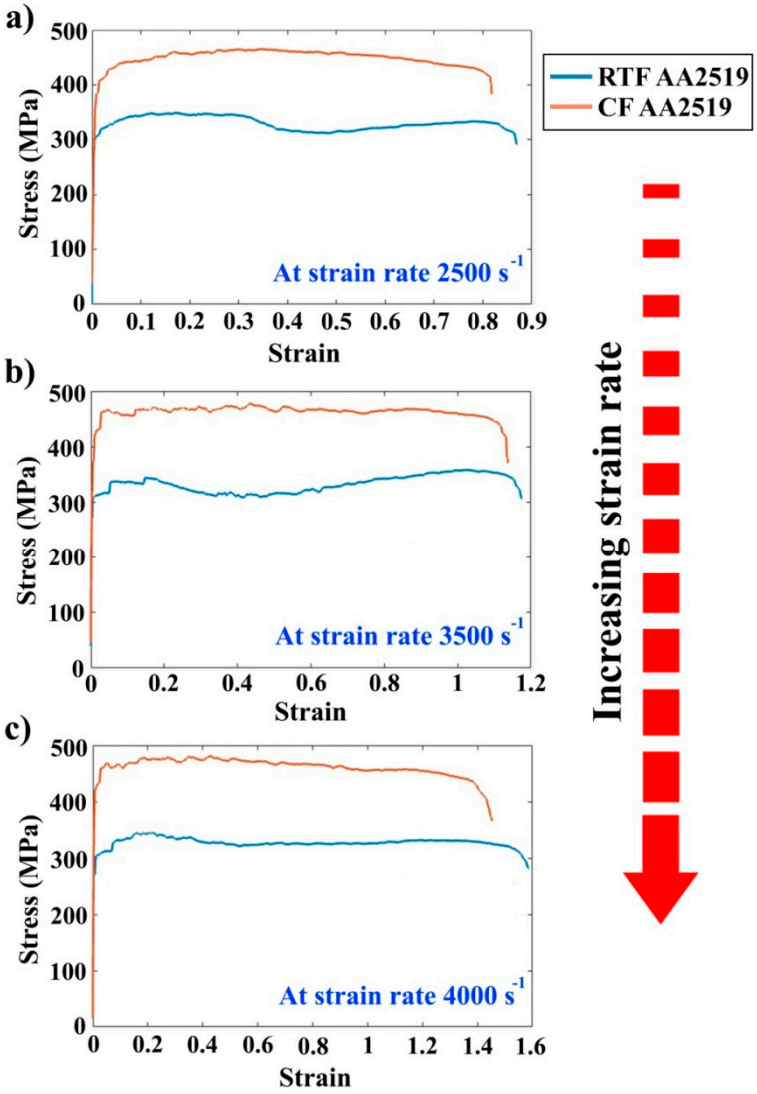


Figure 7. Comparing results of true stress-true strain curves between RTF and CF alloys at (**a**) 2500 s^{-1}; (**b**) 3500 s^{-1}; and (**c**) 4000 s^{-1} strain rates.

The dependency of the flow stress on the applied strain rate is described quantitatively by a coefficient called the strain rate sensitivity (SRS) factor m, which is expressed as [39]

$$m = \left(\frac{\partial \ln \sigma(\varepsilon)}{\partial \ln \dot{\varepsilon}}\right)_{\varepsilon,T} \quad (4)$$

where $\sigma(\varepsilon)$ is the flow stress at a fixed plastic strain and temperature, and $\dot{\varepsilon}$ represents the strain rate. The SRS values in the dynamic high strain rate were determined at 0.1 plastic strain as depicted in the Figure 8a,b for the RTF and CF alloys respectively. Based on the least squares system, the linear fit line of the logarithm of the true stress versus the logarithm of the strain rate plots under the impact loading of the alloys exhibited SRS (m) values of approximately 0.039 for the RTF and 0.055 for the CF processed samples. Higher value of "m" and near-constant SRS plot were reported at high strain rates when

compared to the quasi-static loadings [23]. Thus, higher sensitivity of material to strain rate in the high rates and insensitivity of the materials to strain rate in the quasi-static loading regime are expected. This behavior is attributed to the rate controlling mechanisms changes due to thermomechanical instabilities of the alloys at those rates. In addition, the value of "m" increased when the grain sizes of the specimens were down to ultrafine amounts indicating higher level of sensitivity of CF alloys to strain rates. The transition of the rate-controlling mechanisms is supposed to be mainly responsible for variations of SRS as a function of grain size. Dislocation cutting is the primary mechanism for the flow stress of coarse grained metals whereas grain boundary interactions and sliding are believed to dominate the plastic deformation in UFG materials [40]. Regarding the thermodynamic and kinetic aspects of plastic behavior of the materials, both inter-related SRS and activation volumes of plastic deformation parameters affect the deformation mechanisms.

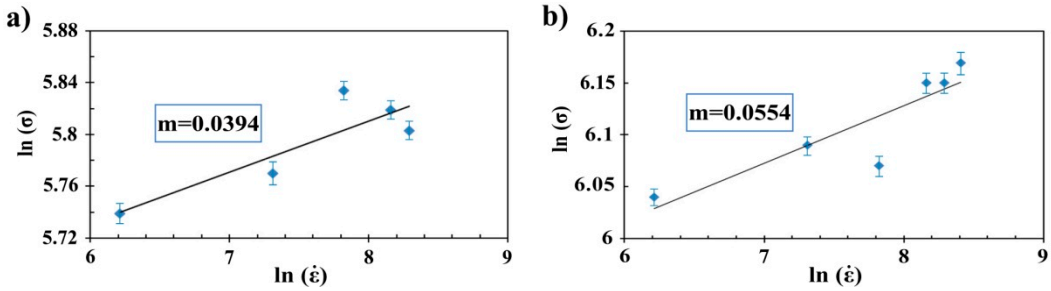


Figure 8. Strain rate sensitivity under dynamic loading related to (**a**) RTF-AA2519 and (**b**) CF-AA2519.

Using the von Mises relation, the SRS can be written in terms of the activation volume and the uniaxial stress in form of the following equation [41]:

$$m = \frac{\sqrt{3}kT}{\sigma \cdot \nu^*} \tag{5}$$

where k and T are the Boltzmann constant and absolute temperature respectively, ν^* is the activation volume and σ shows uniaxial stress. On the other hand, grain size and activation volume parameters have been shown to be directly related to each other such that the activation volume reduces while the grain size decreases [40]. According to Equation (5), the decrease of the activation volume as a result of the grain size reduction leads to the increase in the SRS "m" of the material. Similar results showing higher sensitivity of UFG Al 99.5 (equivalent to AA1050) were reported for low strain rates between 10^{-3} and 10^{-5} s^{-1} by May et. al. [42] when compared to the conventionally grain sized of the aluminum. Su et. al. [40] also observed a considerably enhanced SRS with decreased grain size for aluminum processed by equal channel angular pressing.

3.3. Post-Mortem Microstructure Investigation

As reported, adiabatic shearing is the major failure and fracture mechanism of aluminum alloys at high strain rates [26,43]. Microstructure characterization including second phase particle arrangement, shearing and cracking at highest level of deformation rate in the impacted specimens were discussed in this section. With respect to the different strain rate tested, no evidence of shear band was noticed in the impacted RTF aluminum alloy at strain rates below 4000 s^{-1}. Figure 9 exhibits the micrograph of the RTF-AA2519 alloy deformed at 4000 s^{-1} where it had relatively experienced a notable thermal softening and illustrated heterogeneous deformation leading to the occurrence of adiabatic shear bands (ASBs). The clear boundary between the Al matrix and the ASB can be observed. They are initiated at sites of imperfections and defects in the microstructure and created an area with the higher tendency for cracking. Both types of deformed and transformed shear bands were observed in the optical micrograph of the sample in Figure 9a,b respectively.

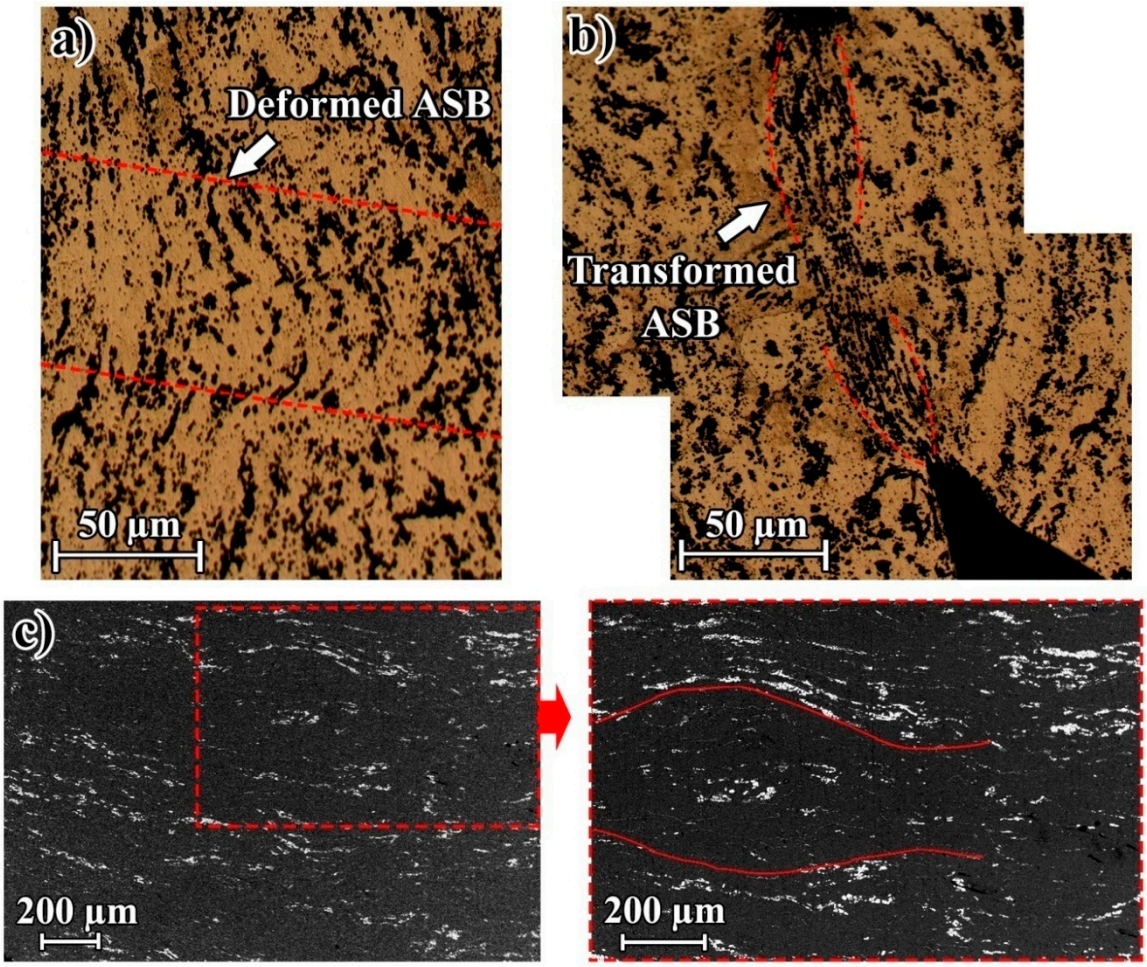


Figure 9. (**a**) Optical micrograph of deformed and (**b**) transformed shear bands and (**c**) SEM and its magnified images of the ASB formed in the RTF-AA2519 alloy.

Normally, ASBs comprise highly distorted grains due to massive strain localization in the region showing a higher tendency to cracking [44,45]. This type of failure is obvious at the ends sides of transformed shear bands in Figure 9b. Moreover, the transformed bands develop from deformed bands as soon as the intensity of the strain localization reaches a critical value [46]. It is also worth noting that the deformed bands are formed in the peripheral regions of the transverse section whereas transformed bands are located in vicinity of the centre area on the impacted specimen. Also, the transformed bands are usually sandwiched by deformed shear bands [47]. This is related to the large temperature gradient generated between the central region and the surface of the specimen as a result of the conversion of the deformation energy into thermal energy during the impact test. Similarly, these sites of forming ASBs were mentioned in the impact study on steel alloys [27]. Thus, it appears that the temperature in the shear band region also plays a significant role in the morphology and type of ASBs formed in the impacted RTF Al alloys.

Figure 9c shows the SEM and its magnified images of the ASB formed in the RTF-AA2519 alloy. It can be seen that the coarse second phase particles appeared to be connected and aligned along with the shear-flow direction indicated in Figure 9c. Because of the high velocity of deformation, the intermetallic particles are seen to have become further elongated and arranged into a band-like pattern with a new configuration which looks like barriers opposing the flow of the material within the evolving band and direction. In this regard, the distance between the second phases (Figure 9c) limits the thickness of formed ASBs in the alloy and increases the localized strain within these bands to strain sufficient to initiate cracks. Furthermore, the second phase particles were pushed aside

by the plastic flow of the soft Al matrix and created a low populated second phase zone inside the shear band. However, it is also expressed that most of the second phase particles inside the ASB appeared to have been dissolved by the intense adiabatic heating and shear strain localization during deformation. In addition, shear band bifurcation was observed in Figure 9c in the alloy. In fact, shear band bifurcations happened since the propagation of a primary shear band along its original direction encountered by a barrier such as impurities or second phase particles. The second phase particles splitting the shear band apart is observable in magnified Figure 9c. To summarize the obtained results, the dynamic behavior of the RTF and CF processed AA2519 alloys are presented in Table 2.

Table 2. Dynamic responses of the RTF and CF processed AA2519.

Materials	Strain Rates (s^{-1})	Maximumflow Stress (MPa)	True Strain at Failure	ASB
RTF-AA2519	500	312	0.09	N/A
	1500	333	0.39	N/A
	2500	348	0.86	N/A
	3500	358	1.16	N/A
	4000	344	1.55	Transformed
CF-AA2519	500	435	0.08	N/A
	1500	463	0.38	N/A
	2500	468	0.79	N/A
	3500	477	1.08	N/A
	4000	480	1.37	N/A
	4500	482	1.62	Deformed

Figure 10 indicates a crack initiated and developed in the transformed shear band which goes through part of the shocked RTF-AA2519 alloy associated with schematics of all crack propagation mechanisms inside the shear bands. All mechanisms of crack development are identified with the arrows in the Figure 10. ASBs have been reported to be the sites where micro-cracks and voids are preferentially nucleated. Four stages have been recognized for the process of crack initiation and propagation inside the ASBs in the forged Al alloys: (1) Formation of microvoids inside the ASBs, (2) coalescence of these microvoids to generate void-clusters elongating to the shear bands' direction, (3) growth and interconnection of contiguous microcracks, (4) microcracks growth and propagation to failure.

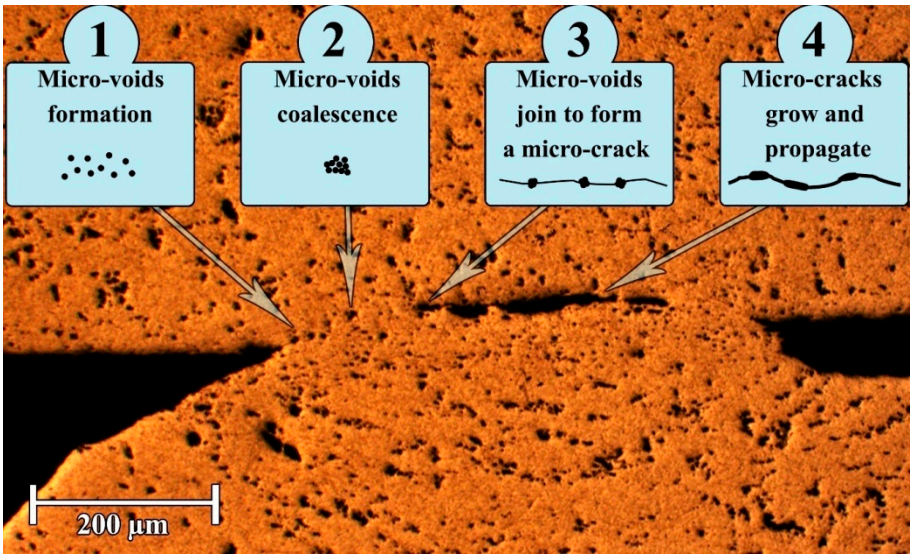


Figure 10. Crack initiation and development in the transformed shear band which goes through part of impacted RTF-AA2519 alloy.

An optical microscopic inspection of the tested CF-AA2519 specimen revealed a circular path in Figure 11a and aligned split arcs in Figure 11b as the various shapes of the deformed ASB. For the first time, these types of ASBs were identified at 4500 s^{-1} when stress–strain curves indicated a slight thermal softening. At the center of the CF specimens, ASBs formed a ring on the compression plane followed by parallel split arcs up, which are extended to the sample surface. The notable point in the impacted CF specimens is that cracks were initiated from the deformed ASB without changing to the transformed state. This phenomenon was of course predictable in dynamic response of CF samples since they showed no drastic thermal softening in their stress–strain curves. A different inelastic deformation mechanism is activated as temperature increases during the expedited post-deformation in UFG aluminum alloys. The large plastic deformation was mostly followed by grain boundary sliding mechanism. It was reported that the ultrafine grain size in aluminum alloys may trigger other deformation mechanisms such as grain boundary interactions and sliding at relatively lower temperature than the defect free bulk counterpart [48]. Therefore, the intergranular crack propagation within ultrafine grains can be accounted as destructive effect that cause failure of the CF samples though there are deformed ASBs at 4500 s^{-1} (Figure 11c). However, it has been proven that the resistance to crack initiation increases with a decrease in the grain size to ultrafine dimensions [49].

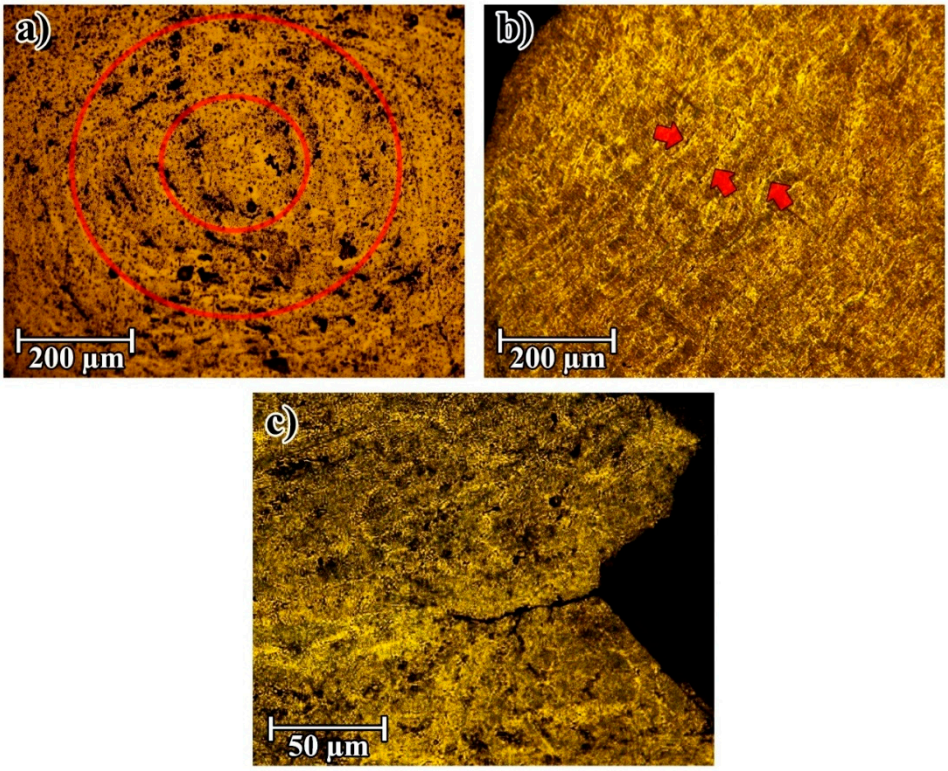


Figure 11. Optical microscopic inspection of (**a**) a circular path and (**b**) aligned split arcs as the various shapes of the deformed ASB and (**c**) propagated crack in the CF-AA2519 specimen.

4. Conclusions

In this research, UFG-AA2519 alloys were synthesized by cryogenic forging technique and its dynamic response at various strain rates was examined. Room temperature forging of the same alloy was also performed to determine the effect of the forging process at cryogenic temperature on the mechanical behavior of the alloy at high strain deformation. In addition, the microstructures of the samples were characterized before as well as after the SHPB impact tests. The main conclusions that can be drawn are summarized as follows:

(1) Microstructure analysis in SEM and OM figures illustrated second phase particles dispersed in a continuous matrix of α-aluminum phase. The particles are irregularly distributed in the RTF matrix, whereas the second phase particles are accumulated and elongated in the shear bands directions in the CF samples. In addition, the aluminum matrix of the CF alloy is more densely populated with fragmented particles when compared to the RTF alloy due to the heavier plastic deformation induced in the material during the cryogenic forging leading to the breaking down of the second phase particles.

(2) The EBSD maps of the deformed RTF and CF samples indicated a significant grain size reduction from ~740 nm to ~250 nm as a result of cryogenic plastic deformation showing higher dislocation densities and stored strains in the CF samples when compared to RTF samples.

(3) The dynamic mechanical response of the RTF and the CF samples were investigated at various high strain rates. Beyond the yield point, there is a stress increment with a declined rate in the plastic part as a result of strain hardening. In the RTF sample, the flow stress was harshly dropped due to thermal softening resulted from thermomechanical instabilities. After 2500 s^{-1}, the RTF-AA2519 alloy indicated a two-stage strain-hardening and flow softening before failure. The multiple peaks in the stress–strain curves can be related to the integrated influence of dislocation accumulation and annihilation due to dynamic recovery. Over 4000 s^{-1}, there is a longer softening step causing the intense drop in the flow stress without any secondary strain hardening. On the other hand, it seems that the CF alloy shows only one flow stress peak consisting of an initial strain hardening such that two strain hardening and thermal softening mechanisms are going almost equally up to the failure. Thus, the thermal softening could not affect the flow stress more than strain hardening in the ultrafine grained alloys. Furthermore, there is no significant increase in the peak flow stress above 3500 s^{-1} in this alloy. In addition, the SRS increased while the grain sizes of the samples were down to the ultrafine grained values exhibiting higher level of sensitivity in the CF alloys to strain rates due to the change in the plastic deformation mechanism to grain boundary interactions.

(4) Deformed and transformed ASBs occurred in the RTF-AA2519 alloy at 4000 s^{-1} strain rate where it had relatively experienced a significant thermal softening. In addition, the crack propagation mechanisms inside the transformed shear band were fully presented. An optical microscopic inspection of the CF-AA2519 revealed a circular path and aligned split arcs as the various shapes of deformed ASB which were seen no earlier than 4500 s^{-1}. The crack major mechanism is also found to be grain boundary sliding such that cracks were initiated from deformed ASB before changing to the transformed state.

Author Contributions: Conceptualization, A.A., N.K. and G.M.O.; methodology, A.A., N.K., G.M.O. and H.F.; materials testing, A.A. and N.K.; characterization, A.A. and H.F.; data analysis, A.A., N.K. and G.W.; writing—original draft preparation, A.A.; writing—review and editing, G.M.O. and G.W; visualization, G.M.O.; supervision, G.M.O. and G.W.; project administration, A.A. and G.M.O.; funding acquisition, G.M.O.

Funding: This research was funded by the ARO, grant number "W911NF-15-1-0457" under the direct supervision of Patricia Huff (HBCU/MI Program Manager, ARO).

Conflicts of Interest: The authors declare no conflict of interest. The funder had no role in the design of the study; in the collection, analyses, or interpretation of data; in the writing of the manuscript, or in the decision to publish the results.

References

1. Gao, Z.; Zhang, X.; Chen, M. Investigation on θ′ precipitate thickening in 2519A-T87 aluminum alloy plate impacted. *J. Alloys Compd.* **2009**, *476*, L1–L3. [CrossRef]
2. Azimi, A.; Shokuhfar, A.; Zolriasatein, A. Nanostructured Al–Zn–Mg–Cu–Zr alloy prepared by mechanical alloying followed by hot pressing. *Mater. Sci. Eng. A* **2014**, *595*, 124–130. [CrossRef]
3. Azimi, A.; Fallahdoost, H.; Nejadseyfi, O. Microstructure, mechanical and tribological behavior of hot-pressed mechanically alloyed Al–Zn–Mg–Cu powders. *Mater. Des.* **2015**, *75*, 1–8. [CrossRef]

4. Zuiko, I.; Kaibyshev, R. Deformation structures and strengthening mechanisms in an Al-Cu alloy subjected to extensive cold rolling. *Mater. Sci. Eng. A* **2017**, *702*, 53–64. [CrossRef]
5. Howeyze, M.; Eivani, A.R.; Arabi, H.; Jafarian, H.R. Effects of deformation routes on the evolution of microstructure, texture and tensile properties of AA5052 aluminum alloy. *Mater. Sci. Eng. A* **2018**, *732*, 120–128. [CrossRef]
6. Immanuel, R.J.; Panigrahi, S.K. Deformation behavior of ultrafine grained A356 material processed by cryorolling and development of Johnson–Cook model. *Mater. Sci. Eng. A* **2018**, *712*, 747–756. [CrossRef]
7. Verlinden, B. Severe plastic deformation of metals. *Metal. J. Metall.* **2005**, *11*, 165–182. [CrossRef]
8. Valiev, R.Z.; Langdon, T.G. Principles of equal-channel angular pressing as a processing tool for grain refinement. *Prog. Mater Sci.* **2006**, *51*, 881–981. [CrossRef]
9. Estrin, Y.; Vinogradov, A. Extreme grain refinement by severe plastic deformation: A wealth of challenging science. *Acta Mater.* **2013**, *61*, 782–817. [CrossRef]
10. Zhilyaev, A.P.; Langdon, T.G. Using high-pressure torsion for metal processing: Fundamentals and applications. *Prog. Mater Sci.* **2008**, *53*, 893–979. [CrossRef]
11. Nejadseyfi, O.; Shokuhfar, A.; Azimi, A.; Shamsborhan, M. Improving homogeneity of ultrafine-grained/nanostructured materials produced by ECAP using a bevel-edge punch. *J. Mater. Sci.* **2015**, *50*, 1513–1522. [CrossRef]
12. Chekhonin, P.; Beausir, B.; Scharnweber, J.; Oertel, C.-G.; Hausöl, T.; Höppel, H.W.; Brokmeier, H.-G.; Skrotzki, W. Confined recrystallization of high-purity aluminium during accumulative roll bonding of aluminium laminates. *Acta Mater.* **2012**, *60*, 4661–4671. [CrossRef]
13. Cherukuri, B.; Srinivasan, R. Properties of AA6061 Processed by Multi-Axial Compressions/Forging (MAC/F). *Mater. Manuf. Process.* **2006**, *21*, 519–525. [CrossRef]
14. Rao, P.N.; Singh, D.; Jayaganthan, R. Mechanical properties and microstructural evolution of Al 6061 alloy processed by multidirectional forging at liquid nitrogen temperature. *Mater. Des.* **2014**, *56*, 97–104. [CrossRef]
15. Dasharath, S.M.; Mula, S. Improvement of mechanical properties and fracture toughness of low SFE Cu-Al alloy through microstructural modification by multiaxial cryoforging. *Mater. Sci. Eng. A* **2017**, *690*, 393–404. [CrossRef]
16. Singh, D.; Jayaganthan, R.; Rao, P.N.; Kumar, A.; Venketeswarlu, D. Effect of the initial grain size on microstructure and mechanical behavior of cryorolled AA5083. *Mater. Today Proc.* **2017**, *4*, 7609–7617. [CrossRef]
17. Vendra, S.S.L.; Goel, S.; Kumar, N.; Jayaganthan, R. A study on fracture toughness and strain rate sensitivity of severely deformed Al 6063 alloys processed by multiaxial forging and rolling at cryogenic temperature. *Mater. Sci. Eng. A* **2017**, *686*, 82–92. [CrossRef]
18. Kumar Singh, A.; Ghosh, S.; Mula, S. Simultaneous improvement of strength, ductility and corrosion resistance of Al2024 alloy processed by cryoforging followed by ageing. *Mater. Sci. Eng. A* **2016**, *651*, 774–785. [CrossRef]
19. Shih, T.-S.; Yong, H.-S.; Hsu, W.-N. Effects of cryogenic forging and anodization on the mechanical properties and corrosion resistance of AA6066–T6 aluminum alloys. *Metals* **2016**, *6*, 51. [CrossRef]
20. Smerd, R.; Winkler, S.; Salisbury, C.; Worswick, M.; Lloyd, D.; Finn, M. High strain rate tensile testing of automotive aluminum alloy sheet. *Int. J. Impact Eng.* **2005**, *32*, 541–560. [CrossRef]
21. Owolabi, G.M.; Bolling, D.T.; Odeshi, A.G.; Whitworth, H.A.; Yilmaz, N.; Zeytinci, A. The Effects of Specimen Geometry on the Plastic Deformation of AA 2219-T8 Aluminum Alloy Under Dynamic Impact Loading. *J. Mater. Eng. Perform.* **2017**, *26*, 5837–5846. [CrossRef]
22. Ye, T.; Li, L.; Guo, P.; Xiao, G.; Chen, Z. Effect of aging treatment on the microstructure and flow behavior of 6063 aluminum alloy compressed over a wide range of strain rate. *Int. J. Impact Eng.* **2016**, *90*, 72–80. [CrossRef]
23. Olasumboye, A.T.; Owolabi, G.M.; Odeshi, A.G.; Yilmaz, N.; Zeytinci, A. Dynamic Behavior of AA2519-T8 Aluminum Alloy Under High Strain Rate Loading in Compression. *J. Dyn. Behav. Mater.* **2018**, *4*, 151–161. [CrossRef]
24. Wright, T.W. 5—Theory of Adiabatic Shear Bands. In *Adiabatic Shear Localization*, 2nd ed.; Dodd, B., Bai, Y., Eds.; Elsevier: Oxford, UK, 2012; pp. 215–246. ISBN 978-0-08-097781-2.
25. Dodd, B.; Bai, Y. *Adiabatic Shear Localization*; Dodd, B., Bai, Y., Eds.; Elsevier: Oxford, UK, 2012; ISBN 978-0-08-097781-2.

26. Tiamiyu, A.A.; Badmos, A.Y.; Odeshi, A.G. Effects of temper condition on high strain-rate deformation of AA 2017 aluminum alloy in compression. *Mater. Des.* **2016**, *89*, 872–883. [CrossRef]
27. Bassim, M.N.; Odeshi, A.G. Shear strain localisation and fracture in high strength structural materials. *Arch. Mater. Sci. Eng.* **2008**, *31*, 69–74.
28. Dorothy, H.L.; Longère, P. Modelling of high strain rate adiabatic shear banding induced failure: A comparison of two approaches. *Int. J. Impact Eng.* **2017**, *110*, 219–227. [CrossRef]
29. Olasumboye, A.; Owolabi, G.; Odeshi, A.; Zeytinci, A.; Yilmaz, N. Dynamic Response and Microstructure Evolution of AA2219-T4 and AA2219-T6 Aluminum Alloys. *J. Dyn. Behav. Mater.* **2018**, *4*, 162–178. [CrossRef]
30. Chen, Y.; Clausen, A.H.; Hopperstad, O.S.; Langseth, M. Application of a split-Hopkinson tension bar in a mutual assessment of experimental tests and numerical predictions. *Int. J. Impact Eng.* **2011**, *38*, 824–836. [CrossRef]
31. Kolsky, H. *Stress Waves in Solids*; Dover Publications: Mineola, NY, USA, 1963.
32. Zuiko, I.S.; Gazizov, M.R.; Kaibyshev, R.O. Effect of thermomechanical treatment on the microstructure, phase composition, and mechanical properties of Al–Cu–Mn–Mg–Zr alloy. *Phys. Met. Metall.* **2016**, *117*, 906–919. [CrossRef]
33. Chen, G.; Fu, G.; Wei, T.; Cheng, C.; Lin, S.; Song, L. Effect of melt treatment on the microstructure and mechanical properties of an AA3003 aluminum alloy. *Mater. Technol.* **2005**, *52*, 583–589. [CrossRef]
34. Nabarro, F. *Plastic deformation and fracture of materials. Edited by Haël Mughrabi, Volume 6 of Materials Science and Technology—A Comprehensive Treatment*; VCH: Weinheim, Germany, 1992; ISBN 3-527-26819-7.
35. Liu, S.; Wang, S.; Ye, L.; Deng, Y.; Zhang, X. Flow behavior and microstructure evolution of 7055 aluminum alloy impacted at high strain rates. *Mater. Sci. Eng. A* **2016**, *677*, 203–210. [CrossRef]
36. Ding, R.; Guo, Z.X. Coupled quantitative simulation of microstructural evolution and plastic flow during dynamic recrystallization. *Acta Mater.* **2001**, *49*, 3163–3175. [CrossRef]
37. Imbert, C.A.C.; McQueen, H.J. Peak strength, strain hardening and dynamic restoration of A2 and M2 tool steels in hot deformation. *Mater. Sci. Eng. A* **2001**, *313*, 88–103. [CrossRef]
38. Hansen, N. Hall–Petch relation and boundary strengthening. *Scr. Mater.* **2004**, *51*, 801–806. [CrossRef]
39. Song, Y.; Guan, Z.; Li, Z.; Wang, M. Theoretical and metrical standardization of strain rate sensitivity index. *Sci. China Ser. E-Technol. Sci.* **2007**, *50*, 714–735. [CrossRef]
40. Su, J.; Tang, Z.; Wang, C.; Ye, T.; Suo, T.; Li, Y. Compressive behavior and deformation kinetics of ultrafine grained aluminum processed by equal channel angular pressing. *Int. J. Smart Nano Mater.* **2017**, *8*, 56–77. [CrossRef]
41. Wei, Q. Strain rate effects in the ultrafine grain and nanocrystalline regimes—Influence on some constitutive responses. *J. Mater. Sci.* **2007**, *42*, 1709–1727. [CrossRef]
42. May, J.; Höppel, H.W.; Göken, M. Strain rate sensitivity of ultrafine-grained aluminium processed by severe plastic deformation. *Scr. Mater.* **2005**, *53*, 189–194. [CrossRef]
43. Odeshi, A.G.; Adesola, A.O.; Badmos, A.Y. Failure of AA 6061 and 2099 aluminum alloys under dynamic shock loading. *Eng. Fail. Anal.* **2013**, *35*, 302–314. [CrossRef]
44. Nesterenko, V.F.; Meyers, M.A.; Wright, T.W. Self-organization in the initiation of adiabatic shear bands. *Acta Mater.* **1998**, *46*, 327–340. [CrossRef]
45. Peirce, D.; Asaro, R.J.; Needleman, A. Material rate dependence and localized deformation in crystalline solids. *Acta Metall.* **1983**, *31*, 1951–1976. [CrossRef]
46. Xu, Y.B.; Zhong, W.L.; Chen, Y.J.; Shen, L.T.; Liu, Q.; Bai, Y.L.; Meyers, M.A. Shear localization and recrystallization in dynamic deformation of 8090 Al–Li alloy. *Mater. Sci. Eng. A* **2001**, *299*, 287–295. [CrossRef]
47. Wang, X. Phenomenon of transformed adiabatic shear band surrounded by deformed adiabatic shear band of ductile metal. *Trans. Nonferrous Met. Soc. China* **2008**, *18*, 1177–1183. [CrossRef]
48. Cho, J.; Li, J.; Li, Q.; Ding, J.; Wang, H.; Xue, S.; Holland, T.B.; Mukherjee, A.K.; Wang, H.; Zhang, X. In-situ high temperature micromechanical testing of ultrafine grained yttria-stabilized zirconia processed by spark plasma sintering. *Acta Mater.* **2018**, *155*, 128–137. [CrossRef]
49. Shukla, S.; Komarasamy, M.; Mishra, R.S. Grain size dependence of fatigue properties of friction stir processed ultrafine-grained Al-5024 alloy. *Int. J. Fatigue* **2018**, *109*, 1–9. [CrossRef]



© 2019 by the authors. Licensee MDPI, Basel, Switzerland. This article is an open access article distributed under the terms and conditions of the Creative Commons Attribution (CC BY) license (http://creativecommons.org/licenses/by/4.0/).